



Visible-light-responsive Cl/S co-doped carbon nitride nanotubes for photocatalytic denitrification: A new reaction pathway dominated by photo-electrons

Guofei Jiang^a, Xuehui You^a, Beiya An^a, Fang Liu^{a,b,c,*}, Xiaoguang Duan^{d,*},
Yongqiang Wang^{a,b,c}, Chunshuang Liu^{a,b,c,d}, Chaocheng Zhao^{a,b,c}

^a College of Chemical Engineering, China University of Petroleum, Qingdao 266580, China

^b State Key Laboratory of Petroleum Pollution Control, Beijing 102206, China

^c State Key Laboratory of Heavy Oil Processing, China University of Petroleum, Qingdao 266580, China

^d School of Chemical Engineering and Advanced Materials, The University of Adelaide, Adelaide, SA 5005, Australia

ARTICLE INFO

Keywords:

Hydrothermal-transverse thermal stripping
Cl/S co-doping
Carbon nitride
Photocatalytic denitrification
Photogenerated electrons

ABSTRACT

In this work, we first applied metal-free polymeric catalysts to drive the photocatalytic denitrification (PCDN) reaction under visible light. We developed a hydrothermal-transverse thermal stripping method to prepare Cl/S co-doped metal-free carbon nitride nanotubes as the photocatalysts (Cl/S-TCN). With larger specific surface area, stronger light response intensity and wider light absorption range, the PCDN performance of Cl/S-TCN was 19 times higher than that of carbon nitride (GCN, obtained by direct calcination of melamine) under visible light. In hole scavenger experiments, the PCDN reaction was dominated by photo-generated electrons (e^-) over Cl/S-TCN in acidic solutions. DFT calculations showed that surface Cl and S dopants preferentially adsorbed the O atoms in NO_3^- and delivered photoinduced- e^- to N atoms through O atoms, ultimately breaking the N-O bond. Such reaction pathway was rarely reported in previous studies. Hence, this work contributes to the first insight into PCDN catalyzed by atomically modified metal-free photocatalyst under visible light.

1. Introduction

Due to the rapid development of chemical, electroplating, paper-making industries and the excessive use of agricultural nitrogen fertilizer, water pollution caused by nitrate (NO_3^-) increasingly threatens ecological balance and human health [1,2], causing water eutrophication and human diseases, such as methemoglobinemia and blue blood [3,4]. Conventional separation technologies (e.g., ion exchange, reverse osmosis or absorption) can separate NO_3^- from wastewater [5–7], but NO_3^- is physically separated and post-treatment is required for managing the concentrated NO_3^- wastewater, causing potential secondary pollution. The biological method is effective for treating NO_3^- wastewater, but the disadvantages are high investment cost and low reaction efficiency which make biotechnology difficult to be applied in small-scale treatment systems [8].

Photocatalysis is a green and sustainable processes and can drive a diversity of redox reactions over semiconducting materials, which is

very promising in wastewater treatment [9,10]. When the photocatalyst is irradiated by light with energy higher than the band gap, the electrons in the valence band (VB) will be excited to enter the conduction band (CB), thereby generating reductive photo-generated electrons (e^-) on CB and leaving oxidizing holes (h^+) on VB [11]. Semiconductor-based photocatalytic denitrification (PCDN) is a new application of photocatalysis in the field of wastewater treatment. Since Kuda reported that TiO_2 can reduce NO_3^- to NH_3 through PCDN [12], a diversity of photocatalytic materials have been developed based on TiO_2 [13–15]. However, TiO_2 has a higher oxidation potential ($E_{\text{VBM}} = 2.7 \text{ V}$) and a lower reduction potential ($E_{\text{CBM}} = -0.5 \text{ V}$) [16], so h^+ oxidation will limit the efficiency of TiO_2 in the PCDN process, and hydroxyl radicals ($\bullet\text{OH}$) with a high oxidation potential (1.8–2.7 V) produced from water oxidation by h^+ also hinders the PCDN reaction [17]. It is an effective strategy to mitigate h^+ oxidation by adding hole scavengers in the PCDN reaction. Small molecule organic acids, such as formic acid [14,18], oxalic acid [19] and acetic acid [15], are commonly used. Their

** Corresponding author at: College of Chemical Engineering, China University of Petroleum, Qingdao 266580, China.

* Corresponding author.

E-mail addresses: liufangfw@upc.edu.cn (F. Liu), xiaoguang.duan@adelaide.edu.au (X. Duan).

carboxylic acid group can be converted by h^+ to $CO_2^{\bullet-}$ with strong reducibility. Most of the PCDN reactions reported so far are dominated by $CO_2^{\bullet-}$ [14,20,21]. PCDN using TiO_2 as catalyst also faces the following challenges. First, e^- plays a small role in PCDN reaction dominated by $CO_2^{\bullet-}$, which makes PCDN rely excessively on the use of hole scavengers, increasing chemical inputs and operating costs. Second, since the $e^- - h^+$ pairs of TiO_2 will recombine very quickly, some current reports accelerate the separation of e^- and h^+ by loading noble metals on the surface of TiO_2 , such as Au [21], Ag [14,22], Pt [23], Pd [24] and other noble metals. The derived composites are expensive and may cause secondary pollution of metal ions. Third, since the band gap of TiO_2 is 3.2 eV, it can only absorb ultraviolet light with wavelength less than 387.5 nm, while visible light occupies 40–50% energy distribution of solar spectrum compared with UV (<8%). According to reports, low-wavelength high-pressure mercury lamp is widely used in the current research based on TiO_2 . In recent years, non- TiO_2 -based photocatalysts have been developed for PCDN, such as $Cu_2O-Cu^0 @Fe^0$ [25] and $Pd/GdCrO_3$ [26], which still use metal-based photocatalysts and high-pressure mercury lamps. To solve the secondary pollution caused by metal dissolution and reduce reaction energy consumption, visible-light-responsive metal-free photocatalyst are promising for e^- -dominant PCDN reaction via band engineering?

As a metal-free organic polymer semiconductor, carbon nitride has a special large π -bond molecular structure hybridized by sp^2 carbon/nitrogen atoms, affording it excellent structural robustness and chemical stability [27,28]. Carbon nitride has a moderate optical band gap (~2.7 eV), which makes it absorb visible light with a wavelength less than 460 nm. The bottom potential of the conduction band of carbon nitride is relatively negative (~−1.1 V), and the top potential of the valence band of carbon nitride is relatively positive (~1.6 V) [29]. Therefore, carbon nitride exhibits high photocatalytic activity in many photocatalytic redox reactions [30,31]. However, there is no report yet on the application of carbon nitride in PCDN. Additionally, pristine carbon nitride also has some inherent shortcomings, such as low specific surface area (SSA) and low photocatalytic activity because of the fast recombination of photogenerated electron-hole pairs [32,33]. Thus, it is very essential to find a suitable method to improve the photocatalytic activity of carbon nitride. Studies have shown that bending carbon nitride into a tubular structure can significantly enlarge its SSA, optimize its electronic structure and band gap, and thus enhance its light absorption and interaction with reactants [34]. The tubular structure can promote multiple reflections of incident light and improve the light utilization on carbon nitride, and the loss of light during reflection is minimized with a lower tube diameter [35]. Moreover, the migration distances of photogenerated carriers from the inside of carbon nitride to the surface are also significantly shorten with a lower tube diameter, and consequently the recombination of photogenerated electron-hole pairs are prohibited [36]. In most of the reported studies, the diameters of the prepared tubular carbon nitride tubes are at the micron level, while the research on the tubular carbon nitride at the nanometer level is rarely reported. In addition to morphology regulation, element doping is also an effective approach to improve the photocatalytic activity of carbon nitride. Particularly, modification carbon nitride with metal-free dopants is favorable in water treatment to avoid metal leaching and associated contamination. In this regard, Cl doping can change the energy band structure through interlayer nesting and adjust the conduction band position of carbon nitride. Meanwhile, due to the higher electronegativity of Cl, it can capture positively charged holes, thereby promoting the separation of photogenerated electron-hole pairs [37]. Additionally, S doping can form a new electron occupying energy level in the valence band, which reduces the band gap of carbon nitride. However, doping single element is normally not sufficient to achieve substantial performance improvement. In view of this limitation, the photocatalytic activity of carbon nitride can be improved by multi-element doping. For example, Cl/S co-doping can make the conduction band position of carbon nitride more negative, enhance the reduction ability of electrons,

and promote the separation of photogenerated electron-hole pairs [38].

In this study, we chose a hydrothermal-transverse thermal stripping method to prepare a metal-free Cl/S-TCN photocatalyst, namely a metal-free Cl/S co-doped carbon nitride nanotubes (Cl/S-TCN). Cl/S-TCN was used a photocatalyst to drive the PCDN reaction under visible light. The well-designed morphology and regulated energy band structure endow Cl/S-TCN with excellent visible light absorption capacity. We revealed that when solution pH was less than 7, the PCDN activity of Cl/S-TCN was mainly dominated by photoinduced e^- . As pH gradually rose, the PCDN reaction was gradually dominated by $CO_2^{\bullet-}$, which was different from the previous reports. Moreover, DFT calculations indicated that Cl and S atoms on the surface of Cl/S-TCN preferentially adsorbed O atoms in NO_3^- and delivered e^- to N, leading to the stepwise removal of O atoms from NO_3^- . This work provides the first report on using metal-free photocatalyst with visible light response for PCDN reactions.

2. Experimental sections

2.1. Preparation of Cl/S co-doped carbon nitride nanotubes

A hydrothermal-transverse thermal stripping method was used to prepare Cl/S co-doped carbon nitride nanotubes. Briefly, 1.29 g of melamine and 1.26 g of cyanuric acid were respectively dissolved into 60 mL of deionized water (50 °C), and the cyanuric acid solution was added into the melamine solution drop by drop. After completely mixing, the resulting product was transferred to a 100 mL Teflon-lined autoclave, and 3 mmol of NH_4Cl and a certain amount of thiourea (1 mmol, 2 mmol, 3 mmol and 4 mmol) were added into the mixture. After reacting at 180 °C for 8 h, the product was separated and calcined at 520 °C under N_2 atmosphere for 4 h (the heating rate was 2 °C/min) to obtain Cl/S co-doped carbon nitride nanotubes. The resulting products were named Cl/S-TCN-x (x = 1, 2, 3 and 4 based on the amounts of thiourea). The preparation process of Cl/S-TCN was shown in Fig. S1. Correspondingly, if NH_4Cl and thiourea were not added into the reactor, the undoped product was recorded as TCN. When a certain amount of NH_4Cl (1 mmol, 2 mmol, 3 mmol and 4 mmol) was added into the reactor, the obtained product was Cl doped carbon nitride nanotubes, which were recorded as Cl-TCN-1, Cl-TCN-2, Cl-TCN-3 and Cl-TCN-4, respectively. When a certain amount of thiourea (1 mmol, 2 mmol, 3 mmol and 4 mmol) was added into the reactor, the obtained product was S doped carbon nitride nanotubes, which were recorded as S-TCN-1, S-TCN-2, S-TCN-3 and S-TCN-4, respectively. There is no use of organic solvents and template agents during the preparation of tubular carbon nitride, making the synthesis safe, green and environmentally friendly. The bulk carbon nitride was obtained by calcinating melamine at 550 °C (under N_2 atmosphere) for 4 h as a control group, recorded as GCN [31, 39]. Characterization details and methodology of density functional theory (DFT) calculations are shown in Supporting Material (Text S1–2).

2.2. Performance test of PCDN

50 mg of photocatalyst was added into 100 mL of 0.8 mmol/L $NaNO_3$ (NO_3^- concentration of 50 mg/L) solution. A 300 W of xenon lamp with a 420 nm cut-off filter was used as the light source, and the reaction was carried out in the reactor as shown in Fig. S2. Before the reaction, the solution was mechanically stirred in dark for 60 min, and argon was introduced into the reactor to remove the dissolved oxygen in the reaction. During the reaction, 3 mL of the reaction solution was taken every 20 min, and the concentration changes of NO_3^- and NO_2^- in the solution were monitored by an ion chromatography, and the concentration changes of NH_4^+ in the solution were monitored by the Nessler method. The used catalyst was filtered and washed 3 times with deionized water, and dried for the next cycle experiment. Since the washing process will cause loss of catalyst, we set up parallel experiments to obtain more used catalyst for the reusability test.

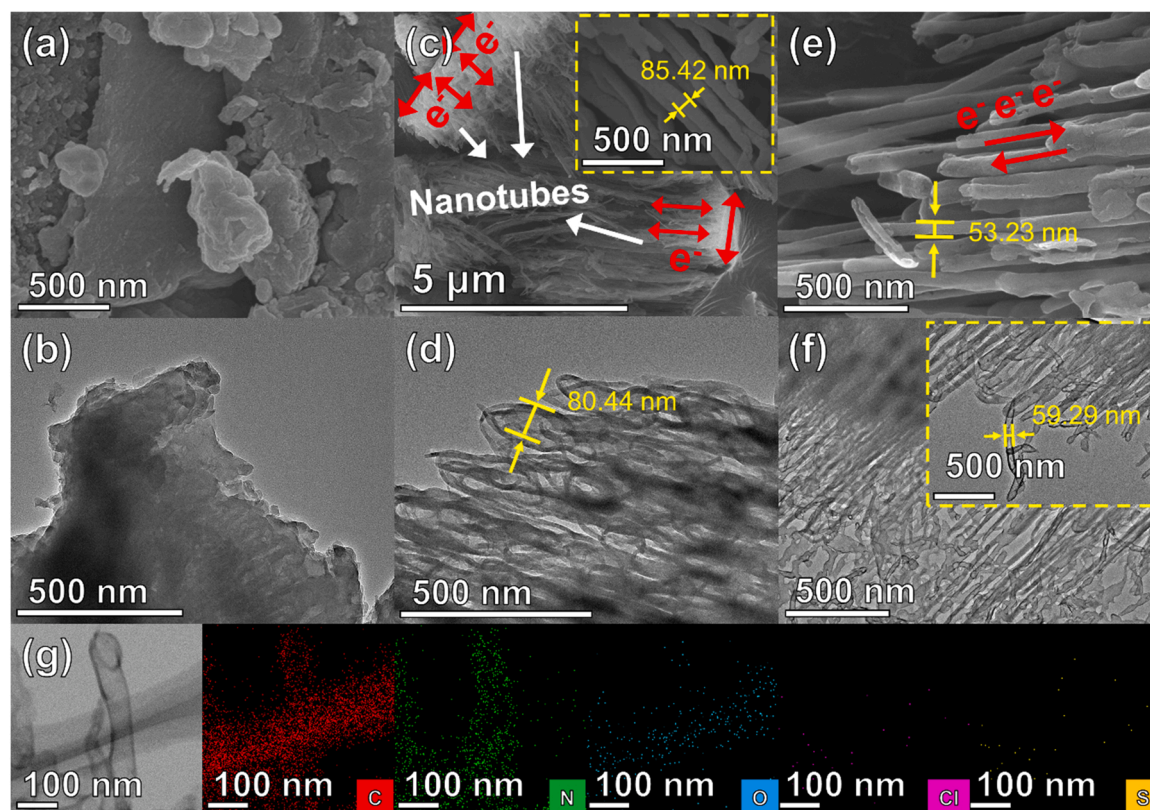


Fig. 1. SEM images of (a) GCN, (c) TCN and (e) Cl/S-TCN-2; TEM images of (b) GCN, (d) TCN and (f) Cl/S-TCN-2; Element mappings diagram of (g) Cl/S-TCN-2.

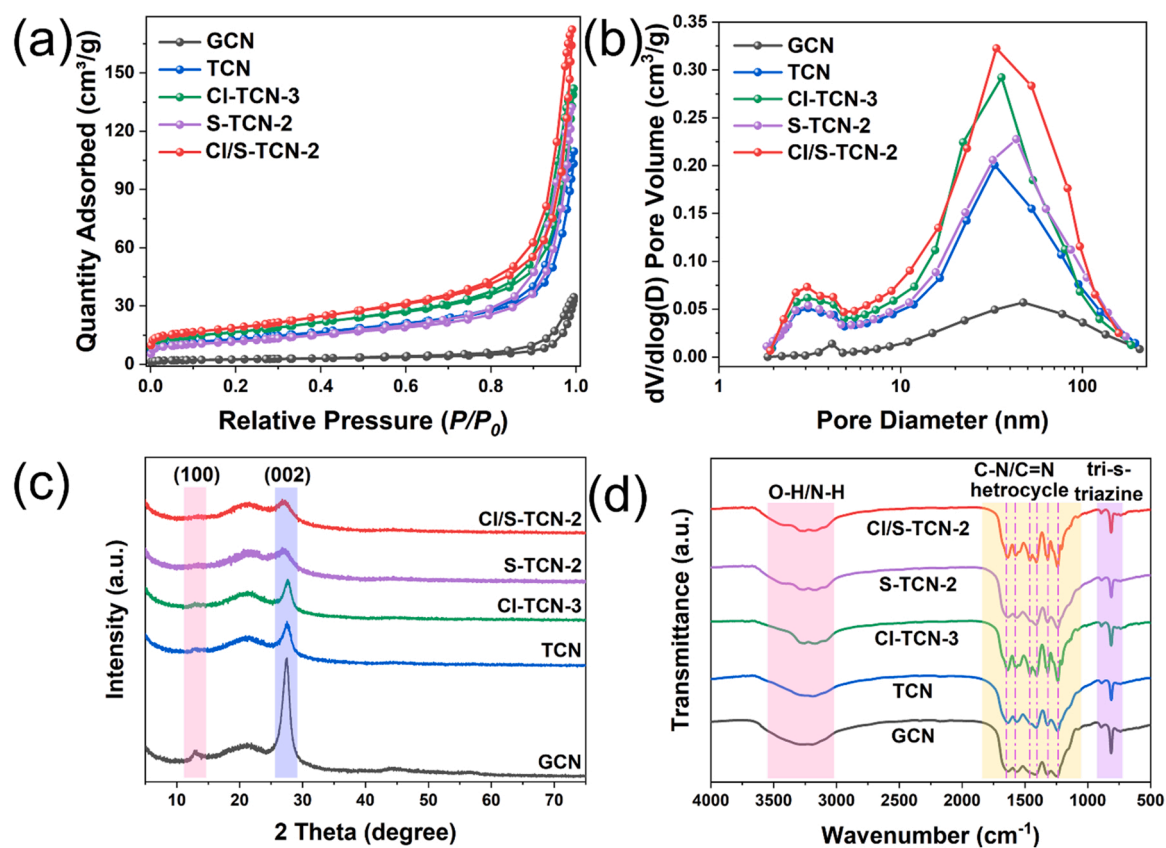


Fig. 2. Diagrams of the prepared catalyst: (a) nitrogen adsorption and desorption isotherm; (b) pore size distribution curve; (c) XRD patterns; (d) FT-IR spectra.

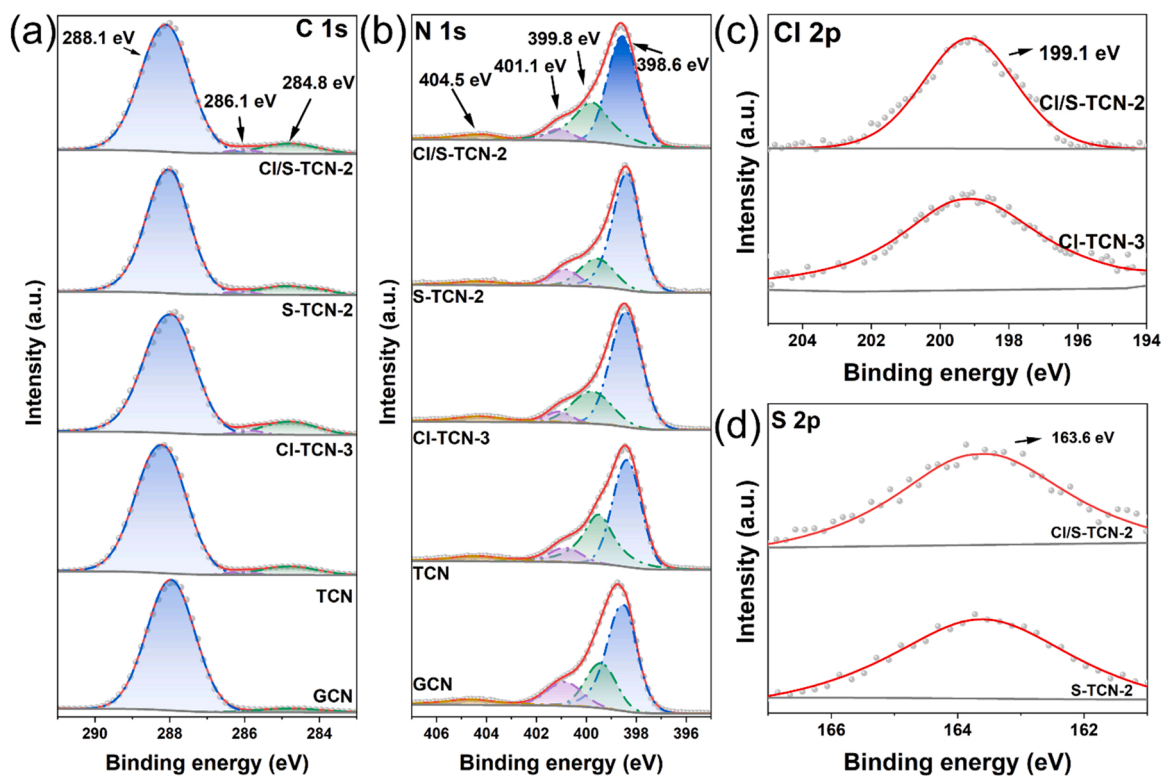


Fig. 3. High-resolution XPS spectra of (a) C 1s, (b) N 1s, (c) Cl 2p and (d) S 2p of the prepared catalyst.

3. Results and discussion

3.1. Catalyst characterization

Different from direct calcination of melamine generating GCN with irregular morphology (Fig. 1a-b), the preparation of Cl/S-TCN by hydrothermal-transverse thermal stripping method underwent multi-step structural changes (Fig. S3). The reaction of melamine with cyanuric acid first produced a white precipitate, which was composed of spherical structures with a diameter of approximately 6–7 μm (Fig. S4a). With the occurrence of hydrothermal reaction, melamine reacted with cyanuric acid by self-assembly, and the spherical structure gradually grew into a hexagonal prism intermediate with $\sim 1 \mu\text{m}$ in diameter (Fig. S4b-c). During calcination, the intermediate was heated and first layered laterally (Fig. S4d). With the extension of calcination time, the internal lamellae gradually transformed into tubing structures with a diameter of about 80–85 nm (Fig. 1c-d). Interestingly, when the intermediate was heated and layered, one end remained the layer structure, resulting in the nanotubes arrayed on a common base plane. Such a structure secured the structural robustness of the prepared TCN (Fig. S4e) and facilitated the rapid transmission of electrons. However, longer-period calcination would destroy the tubular structure (Fig. S4f). The Cl and S doping did not change the morphology of nanotubes, but the diameter of Cl/S-TCN-2 reduced to 53–59 nm (Fig. 1e-f). This is because the Cl and S dopants which a larger atomic radius hindered the molecules binding of melamine and cyanuric acid [40]. A smaller tube diameter often leads to a higher electron transmission rate, thereby improving the photocatalytic efficiency. The element mappings show (Fig. 1g) that Cl/S-TCN-2 is mainly composed of C, N, O, Cl and S. These elements are evenly distributed on the surface of Cl/S-TCN-2, indicating the successful doping of Cl and S.

As we all know, a smaller tube diameter can bring a larger specific surface area, provide more active reaction sites, which help improve the catalytic performance of the materials [41]. N_2 sorption isotherms were used to study the pore structures of the prepared catalysts (Fig. 2a). In

the relative pressure range of 0–1.0, the four samples all conform to the type IV adsorption isotherm of the IUPAC classification standard [42]. The slope and inflection point of the adsorption isotherm indicate that there are many mesoporous structures, which is consistent with the pore size distribution in Fig. 2b. Due to the existence of capillary condensation, the change of adsorption capacity in the low-pressure section is relatively smooth. When P/P_0 increases to 0.85–1.0, the adsorption capacity changes significantly, indicating that all the three samples have H3 hysteresis loops. Table S1 displays the specific surface area, pore volume and pore size distribution of each catalyst. Obviously, Cl/S-TCN-2 has a larger specific surface area ($65.78 \text{ m}^2/\text{g}$), which is 7.97 times higher than that of GCN ($8.25 \text{ m}^2/\text{g}$). Such improvement outperforms the previous reports of co-doped GCN [38,43]. Enlarged SSA is profitable to the adsorption of pollutants and transfer/desorption of reaction products [44].

Fig. 2c shows the XRD patterns of GCN, TCN, Cl-TCN-3, S-TCN-2 and Cl/S-TCN-2. The patterns of all catalysts are similar, indicating that the morphology control and doping did not change the crystal structure of carbon nitride. Compared with GCN, the (100) diffraction peaks of TCN, Cl-TCN-3, S-TCN-2 and Cl/S-TCN-2 almost disappear, and the (002) diffraction peaks become weaker and wider with increased S/Cl doping levels (Fig. S5a). This is because that the defects caused by elemental doping reduce the planar periodicity of carbon nitride [45]. Fig. S5b shows enlarged pictures of the (002) diffraction peaks of different catalysts. Cl doping shifts the (002) diffraction peak to a higher angle, while Cl/S co-doping makes the (002) diffraction peak relocate to a lower angle, indicating that the doping of Cl and S atoms can cause the in-plane spacing of carbon nitride to decrease and increase, respectively. The above is because the electronegativity of Cl atoms (3.16) is greater than that of N atoms (3.04), while the electronegativity of S atoms (2.58) is less than that of N atoms, and different electronegativity will affect the attraction between layers, thereby affecting in-plane spacing [46]. Fig. 2d shows the FT-IR spectrum of the prepared catalysts. The absorption peak at $3000\text{--}3500 \text{ cm}^{-1}$ is caused by the stretching vibration of O-H and N-H, and the peak at 817 cm^{-1} is caused by the breathing

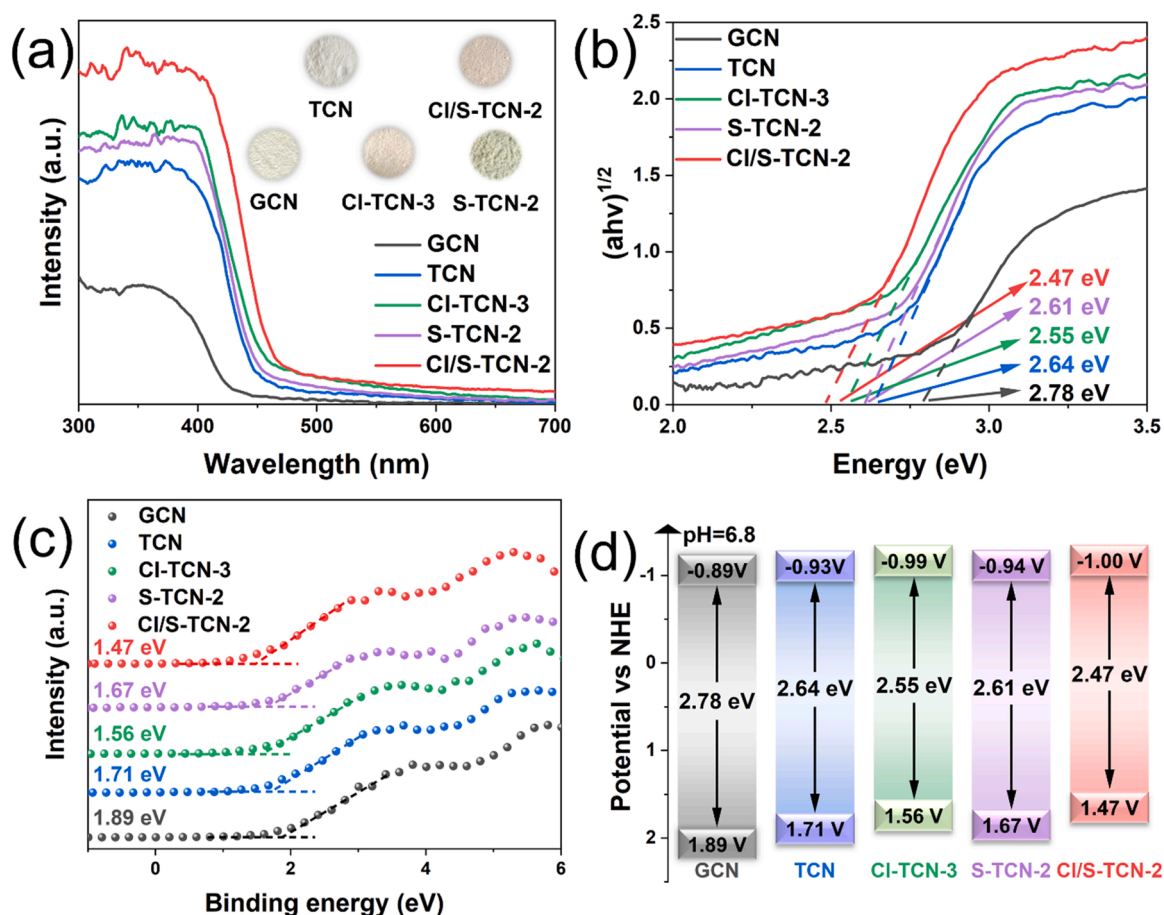


Fig. 4. Pictures of the prepared catalyst: (a) UV-vis diffuse reflection spectra, (b) band gap determination spectrum, (c) XPS valence band map, (d) band gap structure diagram.

mode of tri-s-triazine unit [47]. The absorption peaks at $1145\text{--}1700\text{ cm}^{-1}$ are related to the stretching modes of C-N and C=N heterocycles [48]. It is worth noting that Cl and S doping did not produce new absorption peaks, which is related to the lower content of the dopants.

To further determine the chemical composition and valence state of the prepared catalysts, the XPS spectrum of the catalysts was measured (Fig. S6a). Fig. 3 shows the binding energies of C 1s, N 1s, Cl 2p and S 2p, and all spectra are calibrated with the standard binding energy of C 1s at 284.8 eV. Fig. 3a shows the high-resolution orbital binding energy of C 1s. Two dominant peaks at 284.8 and 288.1 eV are obtained by Gaussian peak fitting, corresponding to graphitic carbons (C-C or C=C) and sp^2 carbons in the tri-s-triazine unit (N-C=N) [49]. A small peak appears at 286.1 eV in C 1s, which corresponds to the C-O bond. However, this peak does not appear in GCN, because the oxygen atom is provided by cyanuric acid. The peak at 532.1 eV in the O 1s spectrum (Fig. S6b) for C-O confirms this statement. In addition, the peaks of TCN, CI-TCN-3, S-TCN-2 and CI/S-TCN-2 at 289.1 eV decrease significantly, which because $-\text{NH}_2$ is partially replaced during the reaction. The XPS spectrum of N 1s (Fig. 3b) is divided into three peaks at 398.6 eV, 399.8 eV and 401.1 eV, corresponding to bridging nitrogen atom (C-N=C), tertiary nitrogen atom (N-(C)3) and amino nitrogen atom (C-N-H) of the tri-s-triazine unit [50]. The peak at 401.1 eV obviously weakens after morphology control and element doping, confirming that amino nitrogen atoms are partially replaced during the reaction. Besides, the peak at 404.5 eV is ascribed to the $\pi\text{-}\pi^*$ excitations between plates. Cl 2p signal was detected in the XPS spectra of CI-TCN-3 and CI/S-TCN-2 (Fig. 3c), the peak at 199.1 eV corresponds to the C-Cl covalent bond, indicating the successful doping of Cl. The peak of S 2p of

CI/S-TCN-2 at 163.6 eV corresponds to C-S-C [51], indicating that S atom replaces N atom and enters the tri-s-triazine unit during the reaction (Fig. 3d). The structure of the catalyst is further revealed by the NMR spectra of solid ^{13}C (Fig. S7). GCN and CI/S-TCN-2 both have two resonance peaks at $\delta_1 = 156.5\text{ ppm}$ and $\delta_2 = 164.5\text{ ppm}$, corresponding to the C atom chemistry shifts of CN_3 and $\text{CN}_2(\text{-NH}_2)$ in the tri-s-triazine unit, respectively [52,53]. Compared with GCN, the ratio of δ_1/δ_2 in CI/S-TCN-2 decreases, indicating the reduction of CN_3 structure and replacement of N by S to form C-S-C. The small peak appearing at $\delta_3 = 160.4\text{ ppm}$ may be related to this. According to the results of XPS and NMR analysis, the structure of the prepared material is inferred (Fig. S8).

The influence of morphology control and elemental doping on the optical properties of carbon nitride was studied by UV-Vis DRS (Fig. 4a). It is clearly seen that GCN shows a typical semiconductor absorption edge at 425 nm, which is consistent with most studies [54]. TCN has a stronger light-trapping ability than GCN, which is related to the better electron-transfer ability of the tubular structure and the more porous structure that can promote multiple reflections of incident light [36]. Besides, Cl and S dopants can further enhance the light-trapping ability of TCN. On the one hand, the doping elements formed donor and acceptor energy levels near the valence band and conduction band. These impurity energy levels acted as the jumping steps of photo-generated electrons in the process of light absorption, thus enhancing the light absorption of TCN. On the other hand, the color of the samples changes from light yellow to gray with increased doping levels (inset of Fig. 4a) [55]. The band gap is calculated by the converted Kubelka-Munk function $((\alpha h\nu)^{1/n} = A(h\nu - E_g))$, where α is absorption index, $h\nu$ is photon energy, E_g is the band gap of a semiconductor. As

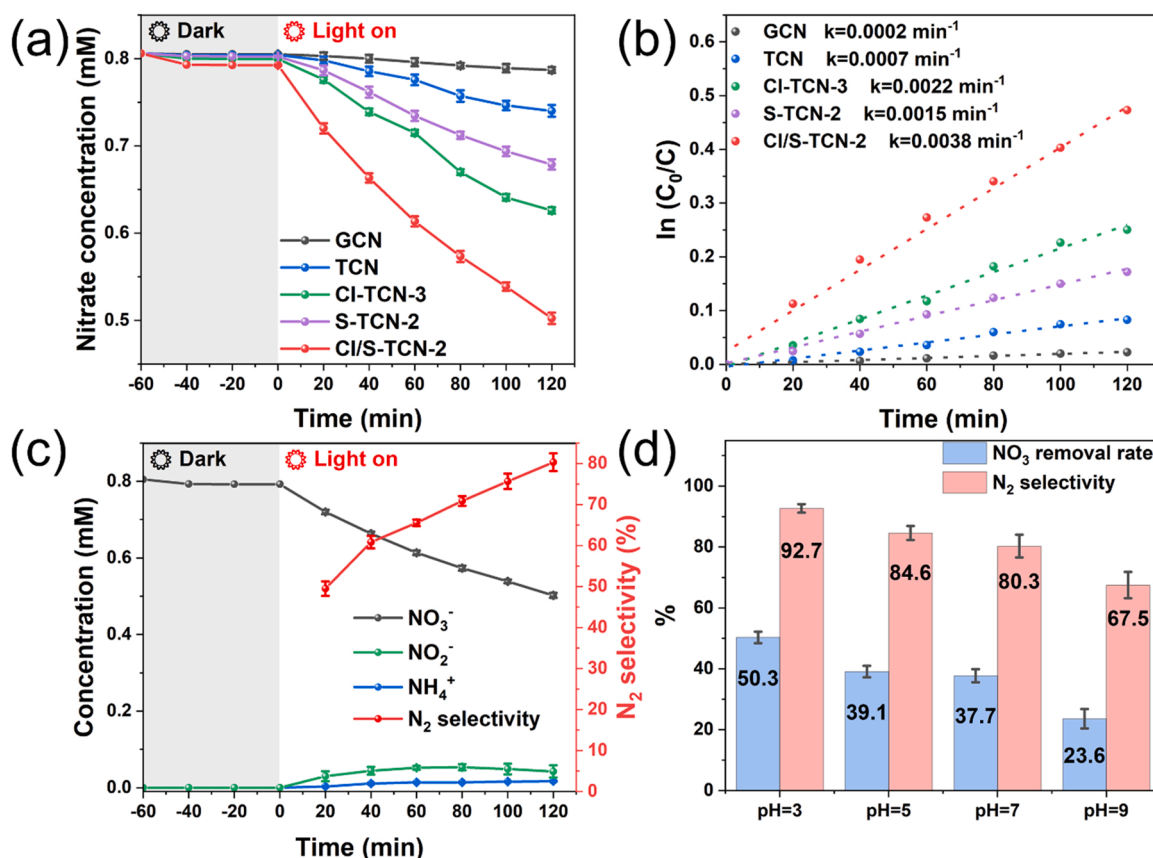


Fig. 5. (a) PCDN performances of different catalysts; (b) First-order-kinetic plots of different catalysts; (c) Changes of various substances in the process of PCDN process of Cl/S-TCN-2; (d) Effects of pH on PCDN performances of Cl/S-TCN-2.

carbon nitride is an indirect bandgap semiconductor, therefore $n = 2$), the band gaps of GCN, TCN, Cl-TCN-3, S-TCN-2 and Cl/S-TCN-2 are 2.78, 2.64, 2.55, 2.61 and 2.47 eV, respectively (Fig. 4b) [56]. Thus, morphology control and elemental doping intensify the absorption and utilization of visible light on GCN. XPS valence band spectra (Fig. 4c) shows that the VB positions of GCN, TCN, Cl-TCN-3, S-TCN-2 and Cl/S-TCN-2 are 1.89, 1.71, 1.56, 1.67 and 1.47 V, and the corresponding E_{CB} are -0.89 , -0.93 , -0.99 , -0.94 and -1.00 V ($E_{CB} = E_{VB} - E_g$). The more negative CB position of Cl/S-TCN-2 indicates stronger reducibility of photoinduced e^- . The band position details of all catalysts are shown in Fig. 4d. DFT calculations show that the lower band gap of Cl/S-TCN is mainly caused by the hybridization of Cl 3p, S 3p and O 2p orbitals with N 2p and C 2p orbitals (Fig. S9).

3.2. PCDN performances of catalysts without hole scavengers

Under simulated visible light, the PCDN performances of different catalysts without hole scavenger were investigated. Fig. 5a shows the PCDN performances of GCN, TCN, Cl-TCN-3, S-TCN-2 and Cl/S-TCN-2 (pH = 7). GCN could only reduce 4.2% of NO_3^- , which was related to the poor light response ability of GCN. The conversion efficiencies of NO_3^- by TCN, Cl-TCN-3, S-TCN-2 and Cl/S-TCN-2 are 8.1%, 22.4%, 15.8% and 37.7%, respectively. The reduction rates of NO_3^- by the four catalysts conformed to the quasi-first-order kinetic model (Fig. 5b). The kinetic constant (k) of NO_3^- reduction by Cl/S-TCN-2 is 0.0038 min^{-1} , which is 19, 5.43, 1.72 and 2.53 times that of GCN, TCN, Cl-TCN-3, and S-TCN-2. The improved conversion efficiency is attributed not only to the morphology control and heteroatom doping that improved the utilization of visible light, but also to the increased photo-electron density in the conduction band induced by Cl and S dopants. These photo-generated electrons migrate to the conduction band to reduce NO_3^- (Eqs.

1–5). However, excessive doping will deteriorate the photocatalytic performance of carbon nitride (Fig. S10). When the concentration of doping elements is too high, the dopants will turn the generated isolated energy levels into recombination centers of photogenerated e^-h^+ pairs, which will reduce the photon yield [57,58]. Additionally, excessive addition of ammonium chloride and thiourea can lead to carbon deposition during thermal exfoliation, which will mask the surface-active sites and result in declined PCDN performance. In the heterogeneous photocatalytic reaction, a higher level of reactant adsorption will reduce the mass transfer distance between semiconductors and pollutants, thereby improving the photocatalytic removal efficiency [11,59]. With a larger specific surface area, the adsorption amount of Cl/S-TCN-2 on NO_3^- is 7.54, 5.77, 2.07 and 3.82 times of GCN, TCN, Cl-TCN-3 and S-TCN-2, respectively (Fig. 5a). Thus, the higher NO_3^- adsorption of Cl/S-TCN-2 accelerates the PCDN performance.



However, the process of PCDN is often accompanied by the production of by-products NO_2^- and NH_4^+ (Eqs. 2–4) as new water pollutants. Thus, the index of N_2 selectivity is particularly important, which can be calculated via Eq. (6):

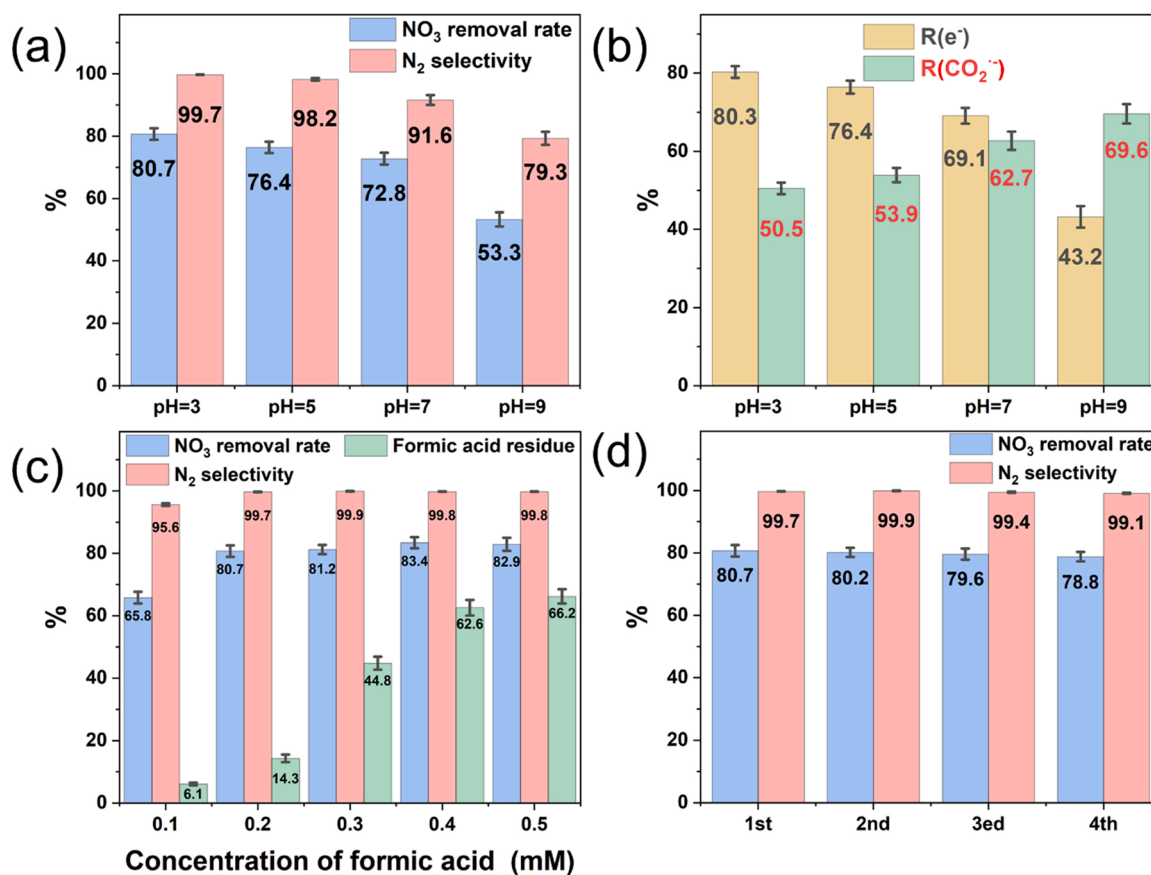


Fig. 6. After adding formic acid: (a) effects of pH on PCDN performances of Cl/S-TCN-2; (b) effects of pH on R(e⁻) and R(CO₂^{•-}); (c) effects of formic acid usage on PCDN performance of Cl/S-TCN-2; (d) stability experiment of PCDN performance.

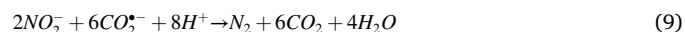
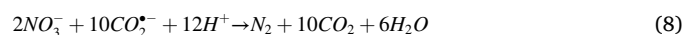
$$S = \frac{[c_{NO_3^-}]_0 - [c_{NO_3^-}]_t - [c_{NO_2^-}]_t - [c_{NH_4^+}]_t}{[c_{NO_3^-}]_0 - [c_{NO_3^-}]_t} \quad (6)$$

where S is N₂ selectivity and c is the molar concentration of the substances. Fig. 5c shows the change trend of N₂ selectivity during the PCDN process of Cl/S-TCN-2. N₂ selectivity increases with the extension of reaction time. The growth rate slowed down after 60 min of reaction, because that NO₂⁻ and NH₄⁺ were re-oxidized to NO₃⁻. After 120 min, the N₂ selectivity of Cl/S-TCN-2 is 80.3%, which is 2.59, 1.34, 1.18 and 1.27 times of GCN, TCN, Cl-TCN-3 and S-TCN-2, respectively (Fig. S11), indicating that Cl/S-TCN-2-induced PCDN process produced fewer by-products. The photocatalytic reaction is often affected by solution pH, and according to Eqs. (1)–(5), H⁺ plays a key role in the PCDN process. In this work, the NO₃⁻ removal rate and the N₂ selectivity over Cl/S-TCN-2 decrease significantly in the pH range of 3–5 and decrease slowly when the pH of the solution further increases to 9 (Fig. 5d). By measuring the zeta potential of Cl/S-TCN-2, the isoelectric point of Cl/S-TCN-2 is 4.63 (Fig. S12). Therefore, when the pH of the solution is less than 4.63, the surface of Cl/S-TCN-2 is protonated and positively charged, which will facilitate the adsorption of NO₃⁻ and improve the photoreduction performance. But when solution pH is higher than 4.63, the negative charge on the surface of Cl/S-TCN-2 will inhibit NO₃⁻ adsorption and increase the mass transfer distance between Cl/S-TCN-2 and NO₃⁻, resulting in significantly inhibited PCDN performance [60,61].

3.3. Effect of hole scavenger on PCDN performance of Cl/S-TCN-2

Adding a certain amount of formic acid to PCDN reaction will consume h⁺ to improve PCDN performance. When 0.2 mM of formic acid was added to the PCDN process and the solution pH was adjusted to

3, the removal rate of NO₃⁻ by Cl/S-TCN-2 increased from 50.3% to 80.7% and the N₂ selectivity increased from 92.7% to 99.7% (Fig. 6a). The main reasons for the enhanced PCDN performance of Cl/S-TCN-2 after adding formic acid are as follows. Firstly, CO₂^{•-} (E(CO₂/CO₂^{•-}) = -1.8 V) generated via the reaction between formic acid and holes would participate photocatalytic reduction (Eqs. 7–9) [25,62]. Secondly, the acidic system constructed by adding formic acid could accelerate the conversion of NO₃⁻ by CO₂^{•-} and e⁻. Thirdly, the addition of formic acid could inhibit the oxidation of NO₂⁻ and NH₄⁺ by h⁺. By analyzing the effects of pH on PCDN performance of Cl/S-TCN-2, we found that under non-alkaline conditions, the addition of formic acid significantly enhanced the stability of PCDN performance of Cl/S-TCN-2. To further study the effects of e⁻ and CO₂^{•-} on the PCDN reaction after adding formic acid, K₂Cr₂O₇ was used as an e⁻ scavenger and methyl viologen was used as CO₂^{•-} scavenger [63]. Eq. (10) was used to calculate the contributions of the two active substances to the photocatalytic reaction kinetics under different pH conditions [64].



$$R(x) = \frac{k(No) - k(x)}{k(No)} \times 100\% \quad (10)$$

where R(x) is the contribution of active substance to photocatalytic degradation kinetics; k(No) is the reaction kinetic constant without scavenger; k(x) is the reaction kinetic constant with scavenger. When the initial pH of the solution is 3, R(e⁻) is significantly higher than R

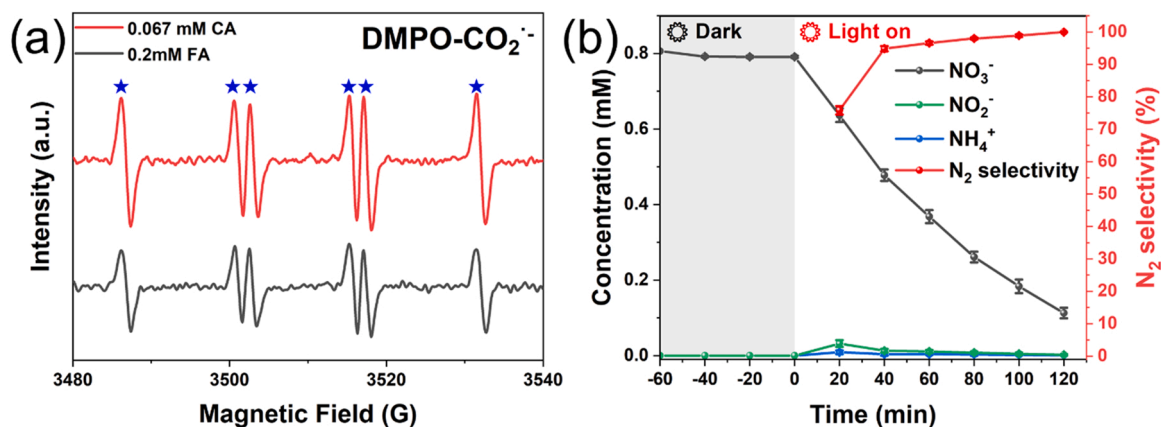


Fig. 7. (a) Effects of different hole scavengers on liquid phase ESR spectra; (b) Changes of various substances in the PCDN process of Cl/S-TCN-2 after adding citric acid.

(CO₂^{•-}) (Fig. 6b), indicating that NO₃⁻ is more prone to adsorbing on the surface of Cl/S-TCN-2 compared with HCOO⁻ under acidic condition, and subsequently reduced by e⁻. With the gradual increase of solution pH, R(CO₂^{•-}) gradually increases. When the pH value is 9, R(CO₂^{•-}) is higher than R(e⁻), suggesting that with the increase of pH value facilitates the adsorption of HCOO⁻ on the surface of Cl/S-TCN-2. Consequently, CO₂^{•-} dominates the reduction reaction. When the initial pH is 3, the solution pH increases with the progress of the reaction (Fig. S13), but the degradation rates only experience slight decreases (Fig. 6a). This indicates that the PCDN process on Cl/S-TCN-2 changes from an e⁻-dominated process to a CO₂^{•-}-dominated process. The reduction process enhances the pH tolerance of Cl/S-TCN-2. The results of this work are different from the previous reports that highly depend on CO₂^{•-}, because the VB potential of Cl/S-TCN-2 is only 1.47 V, which is not capable of oxidizing H₂O to produce •OH. In contrast, the PCDN performance of Cl/S-TCN-2 is better than most of the reported studies, without using metal catalysts and a high-pressure mercury lamp

(Table S2). The PCDN performance of Cl/S-TCN-2 is improved by adding formic acid into the reaction system, but the residual formic acid in water treatment is undesirable. Therefore, it is necessary to study the effect of formic acid concentration on the PCDN performance of Cl/S-TCN-2. Fig. 6c shows that the addition of 0.2 mM of formic acid maximize the conversion of 50 mg/L of NO₃⁻ by Cl/S-TCN-2. Although excessive formic acid could not reduce the conversion rate of NO₃⁻ and N₂ selectivity by PCDN performance of Cl/S-TCN-2, it will generate a large amount of formic acid residue. Therefore, in practical application, formic acid content should be reasonably adjusted according to the NO₃⁻ concentration in wastewater. Cl/S-TCN-2 demonstrates excellent stability of PCDN, and there is no obvious decline in the NO₃⁻ removal rate and N₂ selectivity after four cycles of use (Fig. 6d). Similarly, the XRD pattern of used Cl/S-TCN-2 does not change significantly, indicating that the crystal structure of Cl/S-TCN-2 remains intact during the reaction (Fig. S14).

The above results show that the formation of CO₂^{•-} via Eq. (7)

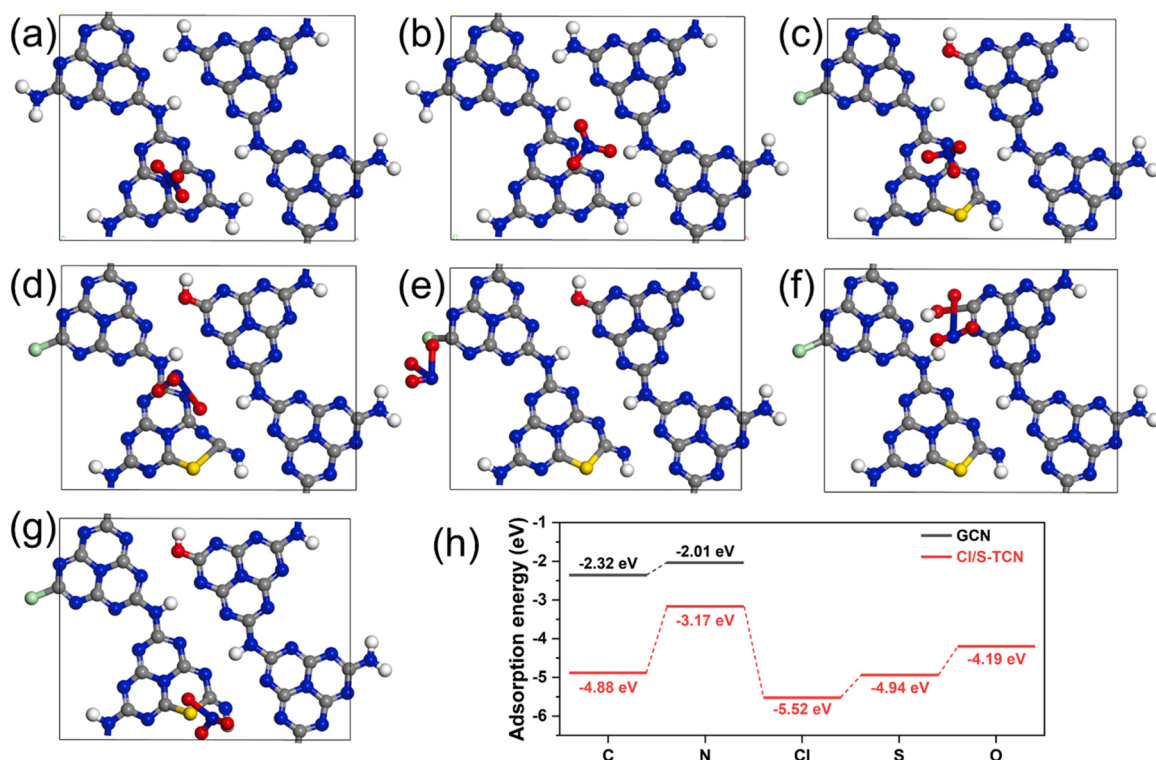


Fig. 8. Adsorption model and (h) adsorption energy of NO₃⁻ by (a, b) GCN and (c-g) Cl/S-TCN.

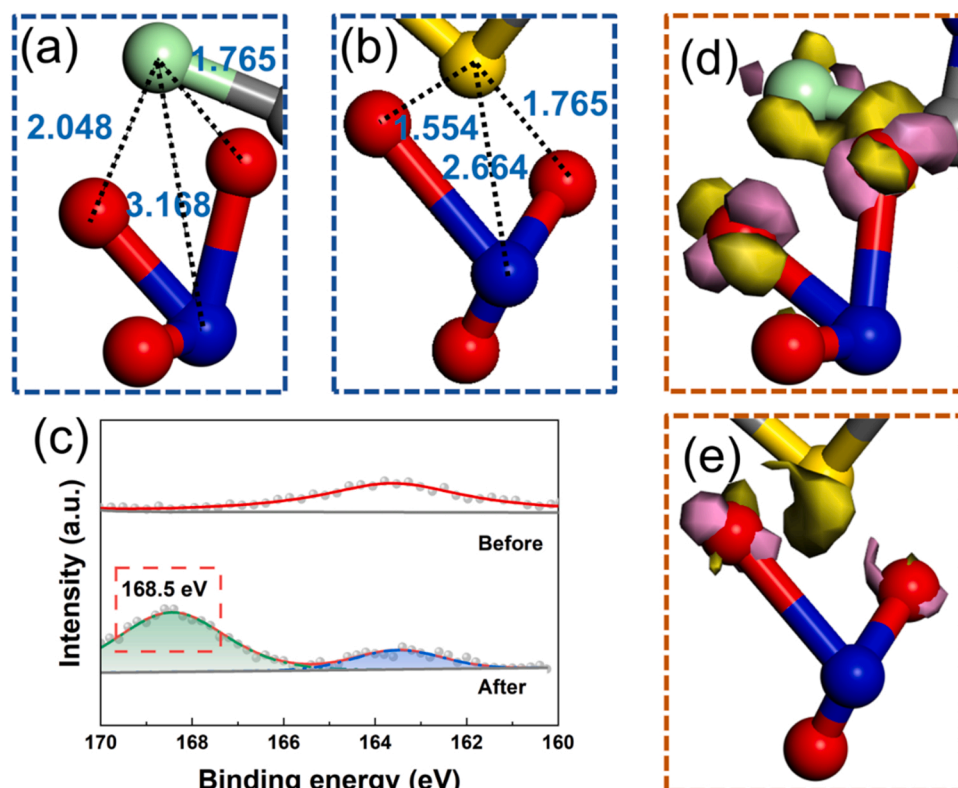


Fig. 9. Distance between NO₃⁻ adsorbed on Cl/S-TCN-2 surface and (a) Cl atoms and (b) S atoms; (c) Comparison of XPS spectrum of S 2p before and after reaction; Differential charge density of NO₃⁻ adsorbed on Cl/S-TCN-2 surface: near (d) Cl atoms and (e) S atoms, the purple and yellow isosurfaces represent the regions of net electron accumulation and deficiency, respectively, and the isosurface value is 0.003 electron/Å³. (For interpretation of the references to colour in this figure, the reader is referred to the web version of this article.)

effectively improved the PCDN performance of Cl/S-TCN-2. So the effects of organic acids containing -COOH on the reduction efficiency of Cl/S-TCN-2 for NO₃⁻ are studied. Citric acid is an important chemical raw material and contains three -COOH. In recent years, soaring amounts of citric acid-containing wastewater are being produced which have caused great challenges to water treatment. This study used citric acid as a hole scavenger to improve the PCDN performance of Cl/S-TCN-2. As shown in ESR results, when the molar concentration of -COOH was the same, the addition of citric acid could produce more CO₂^{•-} during PCDN reaction than formic acid, and the peak intensity was increased to 1.51 times (Fig. 7a). This is because citric acid ($K_a = 7.4 \times 10^{-4}$) has a higher dissociation constant than formic acid ($K_a = 1.8 \times 10^{-4}$), so citric acid can ionize more -COO⁻ in the solution to generate CO₂^{•-} (Fig. S15). Since citric acid itself also has a certain reduction ability, when the adding amount of citric acid is 0.067 mM and the initial pH of is 3, the removal efficiency of NO₃⁻ by Cl/S-TCN-2 reaches 85.9% and N₂ selectivity reaches 99.9% (Fig. 7b). The consumption of citric acid in the reaction is 72.6% (Fig. S16). These results show that the Cl/S-TCN-2 can effectively remove citric acid and NO₃⁻ in wastewater at the same time, achieving the purpose of “treating waste with waste”.

3.4. Enhancement mechanism of PCDN performance of Cl/S-TCN-2

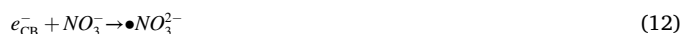
Different from previous studies, e⁻ dominates the PCDN process of Cl/S-TCN-2 at acidic conditions. Since e⁻ is produced by Cl/S-TCN-2, it is particularly important to study the interaction between Cl/S-TCN-2 and NO₃⁻.

3.4.1. Adsorption behaviors of NO₃⁻ by Cl/S-TCN-2

The effects of Cl/S co-doping on the adsorption behaviors of NO₃⁻ by Cl/S-TCN-2 are studied. The following two adsorption models are analyzed by DFT: 1) NO₃⁻ adsorbs on C atoms (Fig. 8a) and N atoms (Fig. 8b) on the surface of GCN; 2) NO₃⁻ adsorbs on C atoms (Fig. 8c), N atoms (Fig. 8d), Cl atoms (Fig. 8e), S atoms (Fig. 8f) and O atoms (Fig. 8g) on the surface of Cl/S-TCN. Among them, the overall

adsorption energy of NO₃⁻ increases from -2.32 and -2.01 eV (on GCN) to -4.88, -3.17, -5.52, -4.94 and -4.19 eV (on Cl/S-GCN) accordingly. The results suggest that the adsorption of NO₃⁻ by Cl/S-TCN was significantly enhanced by Cl/S co-doping (Fig. 8h).

Additionally, during the absorption of NO₃⁻ by Cl/S-TCN-2, Cl and S atoms always have a closer distance with O atoms in NO₃⁻, indicating that the O atoms in NO₃⁻ would preferentially adsorb on Cl and S atoms (Fig. 9a-b). After reaction, XPS spectrum of Cl 2p shifts (Fig. S17), and XPS spectrum of S 2p shows a peak corresponding to S-O at 168.5 eV (Fig. 9c) [65], confirming the above results. Differential charge density is computed to study the charge transfer behaviors of Cl and S atoms to O atoms in NO₃⁻. We found net electron deficiency around the Cl and S dopants and net electron accumulation around O atoms (Fig. 9d-e), indicating that Cl and S atoms on the surface of Cl/S-TCN provide electrons to NO₃⁻ through O atoms. Since the conduction band potential of Cl/S-TCN-2 is -1.00 V, Cl/S-TCN-2 will coordinate the PCDN reaction by e⁻ ($E^\circ(\text{NO}_3^-/\bullet\text{NO}_3^{2-}) = -0.89 \text{ V}$; $E^\circ(\text{NO}_2^-/\bullet\text{NO}_2^{2-}) = -0.47 \text{ V}$; [14,26]). Specifically, photoinduced e⁻ from excited Cl/S-TCN-2 will reach deliver to N through O, subsequently reducing NO₃⁻ and breaking the N-O bond. Thus, the PCDN reaction will stepwise remove O atoms from NO₃⁻ and finally convert NO₃⁻ to N₂. Therefore, PCDN of Cl/S-TCN-2 would not produce NH₄⁺, which is supported by the data in Figs. 5c and 7b. Eqs. (11)–(19) shows the whole process that Cl/S-TCN-2 gradually reduced NO₃⁻ by photo-excited e⁻.



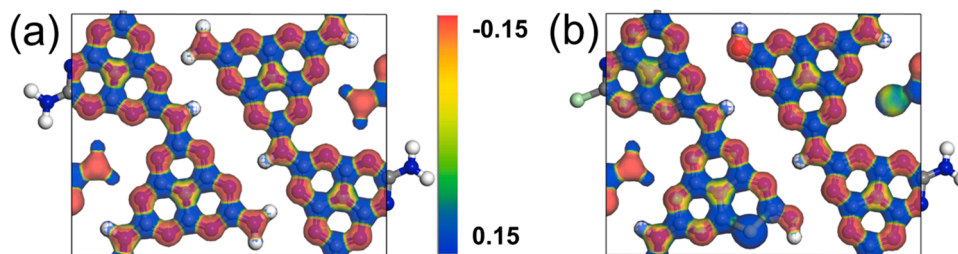


Fig. 10. Electrostatic potential distribution of (a) GCN and (b) Cl/S-TCN-2.

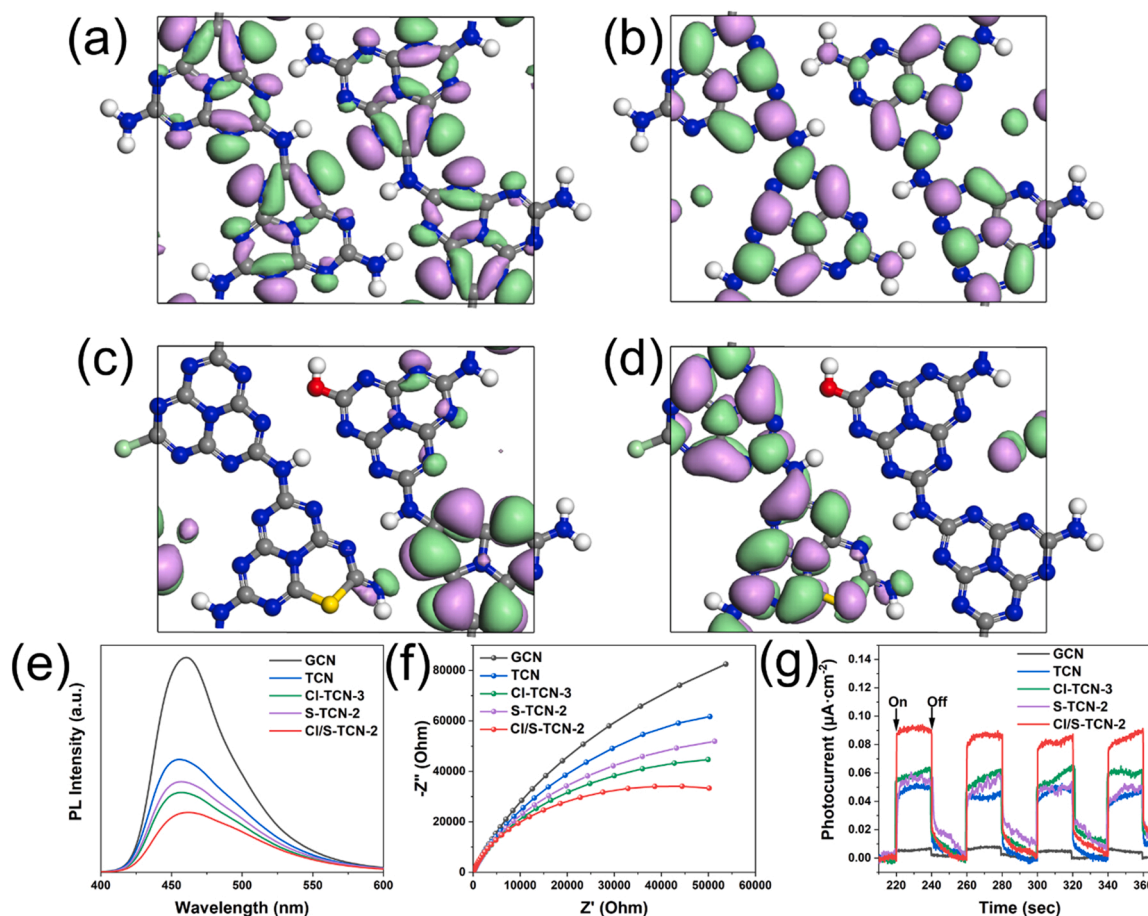


Fig. 11. HOMO orbital of (a) GCN and (c) Cl/S-TCN-2; LUMO orbital of (b) GCN and (d) Cl/S-TCN-2; Diagrams of the prepared catalyst: (e) Photoluminescence spectra; (f) EIS spectra; (g) photocurrent response spectra.



3.4.2. Mechanism of Cl/S-TCN-2 producing e^-

As shown in the electrostatic potential distribution of GCN (Fig. 10a), there are electron-deficient centers (C atoms) and electron-rich centers (N atoms) on the surface. When the visible light irradiates on the surface of GCN, electrons around N atoms transit to the electron-deficient centers, leaving oxidative h^+ at N atoms and reductive e^- at C atoms. Cl/S double doping can adjust the electrostatic potential distribution of Cl/S-TCN-2. As shown in Fig. 10b, electron-deficient centers formed by Cl and

S replace the electron-rich centers of original N atoms, providing Cl/S-TCN-2 with more electron-deficient centers. Therefore, when Cl/S-TCN-2 is excited by visible light: 1) photo-generated electrons will be generated near Cl and S atoms and transfer to the O atoms of NO_3^- ; 2) more electron-deficient centers will reduce the negative effect of hole oxidation on the photocatalytic reduction of NO_3^- .

3.4.3. Photocatalytic enhancement mechanism of Cl/S-TCN-2

HOMO and LUMO orbitals can reveal the mechanism how hetero-atoms affect the separation of photogenerated electron-hole pairs. The HOMO and LUMO orbitals in GCN are uniformly distributed on each atom of GCN (Fig. 11a-b), meaning that the electron-gaining area and the electron-losing area will overlap, which is not conducive to the separation of photogenerated electron-hole pairs. The HOMO and LUMO orbitals of TCN, Cl-TCN-3 and Cl/S-TCN-2 are clearly separated on the left and right, and this high asymmetry can effectively reduce the

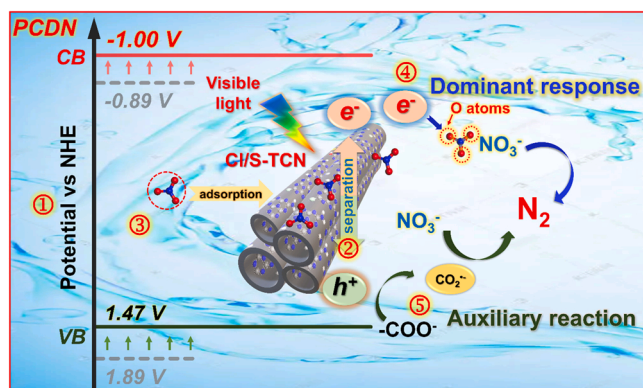


Fig. 12. PCDN mechanism of Cl/S-TCN-2 under visible light.

recombination of photogenerated electron-hole pairs (Fig. 11c-d, Fig. S18).

To better explain the mechanism of the influence of the tubular structure and elemental doping on electron transfer, the photoluminescence spectra, electrochemical impedance and photocurrent response of the catalysts were tested. When the excitation wavelength is 320 nm, all catalysts have a broad emission peak in the range of 400–600 nm (Fig. 11e), and the decrease of emission intensity again proves that morphology control and heteroatom doping effectively inhibit the recombination of photogenerated electrons and holes [66]. Nyquist impedance diagram of the prepared catalysts is shown in Fig. 11f. The Nyquist diagram of all catalysts has only one capacitive reactance arc at high frequency, indicating that there is mainly one charge-transfer process. The charge transfer resistances of GCN, TCN, Cl-TCN-3, S-TCN-2 and Cl/S-TCN-2 are 2.93×10^5 , 1.97×10^5 , 1.16×10^5 , 1.39×10^5 and $8.36 \times 10^4 \Omega$, respectively, indicating that Cl/S-TCN-2 has higher separation efficiency for photogenerated electron-hole pairs and faster interface charge migration [67]. Generally, efficient charge separation often leads to a higher photocurrent density [68]. Compared with that of GCN, the photocurrent responses of TCN, Cl-TCN-3, S-TCN-2 and Cl/S-TCN-2 increase from $0.005 \mu\text{A}\cdot\text{cm}^{-2}$ to 0.049, 0.058, 0.055 and $0.093 \mu\text{A}\cdot\text{cm}^{-2}$, respectively (Fig. 11g). The above results show that the tubular structure and doping with Cl/S are beneficial to improving the separation efficiency of photogenerated electron-hole pairs of carbon nitride, thereby promoting the photocatalytic PCDN performance.

Based on the above discussion, the PCDN mechanism of Cl/S-TCN-2 under visible light irradiation is illustrated in Fig. 12. 1) Cl/S co-doping and the unique tubular structure lead to a reduced band gap of Cl/S-TCN-2 (2.47 eV), affording Cl/S-TCN-2 a wider visible light absorption range; 2) The electron deficient center formed by Cl/S co-doping accelerates the separation of photogenerated electron-hole pairs; 3) Cl/S co-doping enhances the adsorption capacity of Cl/S-TCN-2 for NO_3^- ; 4) Cl/S co-doping results in a more negative CB potential (-1.00 V) of Cl/S-TCN-2. Highly reductive photoinduced- e^- will preferentially destroy the N-O bond of NO_3^- , so that Cl/S-TCN-2 can effectively drive the electron-dominated PCDN reaction under visible light; 5) $\text{CO}_2^{\bullet-}$ generated by the hole scavenger enhances the PCDN performance of Cl/S-TCN-2.

4. Conclusion

In summary, we successfully prepared Cl/S co-doped carbon nitride nanotubes via a hydrothermal-transverse thermal stripping method which efficiently drove the photocatalytic denitrification reaction under visible light irradiation. Cl/S-TCN manifests large specific surface area because of the tubular structures, and Cl/S co-doping regulated the energy band structure of Cl/S-TCN, enabling more negative CB potential and effectively weakening the interference of h^+ on PCDN reaction.

Moreover, Cl/S co-doping enhanced the adsorption of NO_3^- by Cl/S-TCN and promoted the separation of e^-h^+ pairs, achieving a higher PCDN reaction rate compared with unmodified GCN. The PCDN reaction was dominated by photoinduced e^- . The addition of hole scavenger improved the PCDN performance and N_2 selectivity of Cl/S-TCN, because $\text{CO}_2^{\bullet-}$ generated by hole scavenger played an auxiliary role under acidic conditions. The system is promising to treat industrial wastewater that contains citric acid at a natural hole scavenger; in this way, the coupled system will achieve the target of “treating waste with waste”. Overall, this work provides a promising metal-free photocatalyst for denitrification of nitrate wastewater.

CRediT authorship contribution statement

Guofei Jiang: Conceptualization, Data curation, Validation, Writing – original draft, Writing – review & editing. **Xuehui You:** Conceptualization, Material Preparation, Data collection, Investigation. **Beiyi An:** Validation, Investigation. **Fang Liu:** Funding acquisition, Project administration, Supervision, Writing – review & editing. **Yongqiang Wang:** Project administration. **Chunshuang Liu:** Project administration. **Chaocheng Zhao:** Project administration, Resources. **Xiaoguang Duan:** Project administration, Writing – review & editing.

Declaration of Competing Interest

The authors declare that they have no known competing financial interests or personal relationships that could have appeared to influence the work reported in this paper.

Acknowledgments

This work was supported by CNPC safety and environmental protection key technology research and promotion project (2017D-4613), Sub project of National Science and Technology major project (2016ZX05040-003) and China University of Petroleum (East China) Graduate Innovative Engineering Project (YCX2020039).

Appendix A. Supporting information

Supplementary data associated with this article can be found in the online version at doi:10.1016/j.apcatb.2021.121018.

References

- [1] H.O.N. Tugaoen, S. Garcia-Segura, K. Hristovski, P. Westerhoff, Challenges in photocatalytic reduction of nitrate as a water treatment technology, *Sci. Total Environ.* 599–600 (2017) 1524–1551.
- [2] F.T. Wakida, D.N. Lerner, Non-agricultural sources of groundwater nitrate: a review and case study, *Water Res.* 39 (2005) 3–16.
- [3] N. Barrabés, J. Sá, Catalytic nitrate removal from water, past, present and future perspectives, *Appl. Catal. B* 104 (2011) 1–5.
- [4] A. Sowmya, S. Meenakshi, Photocatalytic reduction of nitrate over Ag-TiO₂ in the presence of oxalic acid, *J. Water Process. Eng.* 8 (2015) e23–e30.
- [5] A. Bhatnagar, M. Sillanpää, A review of emerging adsorbents for nitrate removal from water, *Chem. Eng. J.* 168 (2011) 493–504.
- [6] Y.A. Shaban, A.A. El Maradny, R.K. Al Farawati, Photocatalytic reduction of nitrate in seawater using C/TiO₂ nanoparticles, *J. Photochem. Photobiol. A* 328 (2016) 114–121.
- [7] X. Xu, B.-Y. Gao, Q.-Y. Yue, Q.-Q. Zhong, Preparation of agricultural by-product based anion exchanger and its utilization for nitrate and phosphate removal, *Bioresour. Technol.* 101 (2010) 8558–8564.
- [8] J.P. Bassin, R. Kleerebezem, M. Dezotti, M.C.M. van Loosdrecht, Simultaneous nitrogen and phosphate removal in aerobic granular sludge reactors operated at different temperatures, *Water Res.* 46 (2012) 3805–3816.
- [9] A. Kumar, P. Raizada, A. Hosseini-Bandegharai, V.K. Thakur, V.-H. Nguyen, P. Singh, C., N-Vacancy defect engineered polymeric carbon nitride towards photocatalysis: viewpoints and challenges, *J. Mater. Chem. A* 9 (2021) 111–153.
- [10] S. Patial, P. Raizada, V. Hasija, P. Singh, V.K. Thakur, V.H. Nguyen, Recent advances in photocatalytic multivariate metal organic frameworks-based nanostructures toward renewable energy and the removal of environmental pollutants, *Mater. Today Energy* 19 (2021), 100589.

- [11] A. Kumar, P. Raizada, P. Singh, R.V. Saini, A.K. Saini, A. Hosseini-Bandegharai, Perspective and status of polymeric graphitic carbon nitride based Z-scheme photocatalytic systems for sustainable photocatalytic water purification, *Chem. Eng. J.* 391 (2020), 123496.
- [12] A. Kudo, K. Domen, K.-i. Maruya, T. Onishi, Photocatalytic reduction of NO_3^- to form NH_3 over Pt-TiO₂, *Chem. Lett.* 16 (1987) 1019–1022.
- [13] K. Doudrick, T. Yang, K. Hristovski, P. Westerhoff, Photocatalytic nitrate reduction in water: managing the hole scavenger and reaction by-product selectivity, *Appl. Catal. B* 136–137 (2013) 40–47.
- [14] H.-T. Ren, S.-Y. Jia, J.-J. Zou, S.-H. Wu, X. Han, A facile preparation of $\text{Ag}_2\text{O}/\text{P25}$ photocatalyst for selective reduction of nitrate, *Appl. Catal. B* 176–177 (2015) 53–61.
- [15] J. Sá, C.A. Agüera, S. Gross, J.A. Anderson, Photocatalytic nitrate reduction over metal modified TiO₂, *Appl. Catal. B* 85 (2009) 192–200.
- [16] M. Shand, J.A. Anderson, Aqueous phase photocatalytic nitrate destruction using titania based materials: routes to enhanced performance and prospects for visible light activation, *Catal. Sci. Technol.* 3 (2013) 879–899.
- [17] G. Liu, S. You, M. Ma, H. Huang, N. Ren, Removal of nitrate by photocatalytic denitrification using nonlinear optical material, *Environ. Sci. Technol.* 50 (2016) 11218–11225.
- [18] F. Zhang, R. Jin, J. Chen, C. Shao, W. Gao, L. Li, N. Guan, High photocatalytic activity and selectivity for nitrogen in nitrate reduction on Ag/TiO_2 catalyst with fine silver clusters, *J. Catal.* 232 (2005) 424–431.
- [19] H. Adamu, A.J. McCue, R.S.F. Taylor, H.G. Manyar, J.A. Anderson, Simultaneous photocatalytic removal of nitrate and oxalic acid over $\text{Cu}_2\text{O}/\text{TiO}_2$ and $\text{Cu}_2\text{O}/\text{TiO}_2$ -AC composites, *Appl. Catal. B* 217 (2017) 181–191.
- [20] A. Devadas, S. Vasudevan, F. Epron, Nitrate reduction in water: influence of the addition of a second metal on the performances of the Pd/CeO_2 catalyst, *J. Hazard. Mater.* 185 (2011) 1412–1417.
- [21] J.A. Anderson, Photocatalytic nitrate reduction over Au/TiO_2 , *Catal. Today* 175 (2011) 316–321.
- [22] D. Sun, W. Yang, L. Zhou, W. Sun, Q. Li, J.K. Shang, The selective deposition of silver nanoparticles onto {101} facets of TiO_2 nanocrystals with co-exposed {001}/ {101} facets, and their enhanced photocatalytic reduction of aqueous nitrate under simulated solar illumination, *Appl. Catal. B* 182 (2016) 85–93.
- [23] L. Li, Z. Xu, F. Liu, Y. Shao, J. Wang, H. Wan, S. Zheng, Photocatalytic nitrate reduction over Pt-Cu/TiO₂ catalysts with benzene as hole scavenger, *J. Photochem. Photobiol. A Chem.* 212 (2010) 113–121.
- [24] R. Molinari, C. Lavarato, P. Argurio, Photocatalytic reduction of acetophenone in membrane reactors under UV and visible light using TiO_2 and Pd/TiO_2 catalysts, *Chem. Eng. J.* 274 (2015) 307–316.
- [25] D. Zhang, B. Wang, X. Gong, Z. Yang, Y. Liu, Selective reduction of nitrate to nitrogen gas by novel $\text{Cu}_2\text{O}-\text{Cu}^0/\text{Fe}^0$ composite combined with HCOOH under UV radiation, *Chem. Eng. J.* 359 (2019) 1195–1204.
- [26] Z. Hou, F. Chen, J. Wang, C.P. François-Xavier, T. Wintgens, Novel Pd/GdCrO_3 composite for photo-catalytic reduction of nitrate to N_2 with high selectivity and activity, *Appl. Catal. B* 232 (2018) 124–134.
- [27] D. Masih, Y. Ma, S. Rohani, Graphitic C_3N_4 based noble-metal-free photocatalyst systems: a review, *Appl. Catal. B* 206 (2017) 556–588.
- [28] C. Jin-Bao, L. Kai-Ning, L. Xiao-Fang, F. Jia-Jie, L. Kang-Le, Preparation and modification of crystalline carbon nitride, *Chinese, J. Inorg. Chem.* 37 (2021) 1713–1726.
- [29] Z. Tong, D. Yang, Y. Sun, Y. Nan, Z. Jiang, Tubular $\text{g-C}_3\text{N}_4$ isotype heterojunction: enhanced visible-light photocatalytic activity through cooperative manipulation of oriented electron and hole transfer, *Small* 12 (2016) 4093–4101.
- [30] M. Li, L. Zhang, X. Fan, M. Wu, Y. Du, M. Wang, Q. Kong, L. Zhang, J. Shi, Dual synergistic effects in $\text{MoS}_2/\text{pyridine-modified g-C}_3\text{N}_4$ composite for highly active and stable photocatalytic hydrogen evolution under visible light, *Appl. Catal. B* 190 (2016) 36–43.
- [31] K. Li, X. Ou, R. Li, Q. Li, J. Fan, K. Lv, Strategies for the fabrication of 2D carbon nitride nanosheets, *Acta Phys. Chim. Sin.* 37 (2021), 2008010.
- [32] L. Lin, Z. Lin, J. Zhang, X. Cai, W. Lin, Z. Yu, X. Wang, Molecular-level insights on the reactive facet of carbon nitride single crystals photocatalysing overall water splitting, *Nat. Catal.* 3 (2020) 649–655.
- [33] X. Li, Z. Hu, Q. Li, M. Lei, J. Fan, S.A.C. Carabineiro, Y. Liu, K. Lv, Three in one: atomically dispersed Na boosting the photoreactivity of carbon nitride towards NO oxidation, *Chem. Comm.* 56 (2020) 14195–14198.
- [34] S. Guo, Y. Tang, Y. Xie, C. Tian, Q. Feng, W. Zhou, B. Jiang, P-doped tubular $\text{g-C}_3\text{N}_4$ with surface carbon defects: universal synthesis and enhanced visible-light photocatalytic hydrogen production, *Appl. Catal. B* 218 (2017) 664–671.
- [35] W. Wang, Z. Zeng, G. Zeng, C. Zhang, R. Xiao, C. Zhou, W. Xiong, Y. Yang, L. Lei, Y. Liu, D. Huang, M. Cheng, Y. Yang, Y. Fu, H. Luo, Y. Zhou, Sulfur doped carbon quantum dots loaded hollow tubular $\text{g-C}_3\text{N}_4$ as novel photocatalyst for destruction of *Escherichia coli* and tetracycline degradation under visible light, *Chem. Eng. J.* 378 (2019), 122132.
- [36] Y.-J. Yuan, Z. Shen, S. Wu, Y. Su, L. Pei, Z. Ji, M. Ding, W. Bai, Y. Chen, Z.-T. Yu, Z. Zou, Liquid exfoliation of $\text{g-C}_3\text{N}_4$ nanosheets to construct $^2\text{D}-^2\text{D}$ $\text{MoS}_2/\text{g-C}_3\text{N}_4$ photocatalyst for enhanced photocatalytic H_2 production activity, *Appl. Catal. B* 246 (2019) 120–128.
- [37] D. Wang, X. Huang, Y. Huang, X. Yu, Y. Lei, X. Dong, Z. Su, Self-assembly synthesis of petal-like Cl-doped $\text{g-C}_3\text{N}_4$ nanosheets with tunable band structure for enhanced photocatalytic activity, *Colloids Surf. A Physicochem. Eng. Asp.* 611 (2021), 125780.
- [38] X. Li, J. Zhang, Y. Huo, K. Dai, S. Li, S. Chen, Two-dimensional sulfur- and chlorine-codoped $\text{g-C}_3\text{N}_4/\text{CdSe}$ -amine heterostructures nanocomposite with effective interfacial charge transfer and mechanism insight, *Appl. Catal. B* 280 (2021), 119452.
- [39] Y. Li, M. Gu, X. Zhang, J. Fan, K. Lv, S.A.C. Carabineiro, F. Dong, 2D $\text{g-C}_3\text{N}_4$ for advancement of photo-generated carrier dynamics: status and challenges, *Mater. Today* 41 (2020) 270–303.
- [40] S. Wang, F. He, X. Zhao, J. Zhang, Z. Ao, H. Wu, Y. Yin, L. Shi, X. Xu, C. Zhao, Phosphorus doped carbon nitride nanobelts for photodegradation of emerging contaminants and hydrogen evolution, *Appl. Catal. B* 257 (2019), 117931.
- [41] C. Zhu, X. Chen, J. Ma, C. Gu, Q. Xian, T. Gong, C. Sun, Carbon nitride-modified defective $\text{TiO}_2-x/\text{carbon spheres}$ for photocatalytic H_2 Evolution and pollutants removal: synergistic effect and mechanism insight, *J. Phys. Chem. C* 122 (2018) 20444–20458.
- [42] M. Wu, J. Zhang, B.-b. He, H.-w. Wang, R. Wang, Y.-s. Gong, In-situ construction of coral-like porous P-doped $\text{g-C}_3\text{N}_4$ tubes with hybrid 1D/2D architecture and high efficient photocatalytic hydrogen evolution, *Appl. Catal. B* 241 (2019) 159–166.
- [43] F. Yi, H. Gan, H. Jin, W. Zhao, K. Zhang, H. Jin, H. Zhang, Y. Qian, J. Ma, Sulfur- and chlorine-co-doped $\text{g-C}_3\text{N}_4$ nanosheets with enhanced active species generation for boosting visible-light photodegradation activity, *Sep. Purif. Technol.* 233 (2020), 115997.
- [44] F. Dong, Z. Zhao, Y. Sun, Y. Zhang, S. Yan, Z. Wu, An advanced semimetal-organic Bi Spheres- $\text{g-C}_3\text{N}_4$ nanohybrid with SPR-enhanced visible-light photocatalytic performance for NO purification, *Environ. Sci. Technol.* 49 (2015) 12432–12440.
- [45] W. Wang, Q. Niu, G. Zeng, C. Zhang, D. Huang, B. Shao, C. Zhou, Y. Yang, Y. Liu, H. Guo, W. Xiong, L. Lei, S. Liu, H. Yi, S. Chen, X. Tang, 1D porous tubular $\text{g-C}_3\text{N}_4$ capture black phosphorus quantum dots as 1D/0D metal-free photocatalysts for oxytetracycline hydrochloride degradation and hexavalent chromium reduction, *Appl. Catal. B* 273 (2020), 119051.
- [46] X. She, L. Liu, H. Ji, Z. Mo, Y. Li, L. Huang, D. Du, H. Xu, H. Li, Template-free synthesis of 2D porous ultrathin nonmetal-doped $\text{g-C}_3\text{N}_4$ nanosheets with highly efficient photocatalytic H_2 evolution from water under visible light, *Appl. Catal. B* 187 (2016) 144–153.
- [47] K. Li, X. Xie, W.-D. Zhang, Porous graphitic carbon nitride derived from melamine-ammonium oxalate stacking sheets with excellent photocatalytic hydrogen evolution activity, *ChemCatChem* 8 (2016) 2128–2135.
- [48] Y. Yang, C. Zhang, D. Huang, G. Zeng, J. Huang, C. Lai, C. Zhou, W. Wang, H. Guo, W. Xue, R. Deng, M. Cheng, W. Xiong, Boron nitride quantum dots decorated ultrathin porous $\text{g-C}_3\text{N}_4$: Intensified exciton dissociation and charge transfer for promoting visible-light-driven molecular oxygen activation, *Appl. Catal. B* 245 (2019) 87–99.
- [49] H. Li, C. Shan, B. Pan, Fe(III)-doped $\text{g-C}_3\text{N}_4$ mediated peroxymonosulfate activation for selective degradation of phenolic compounds via high-valent iron-oxo species, *Environ. Sci. Technol.* 52 (2018) 2197–2205.
- [50] Q. Zheng, D.P. Durkin, J.E. Elenewski, Y. Sun, N.A. Banek, L. Hua, H. Chen, M. J. Wagner, W. Zhang, D. Shuai, Visible-light-responsive graphitic carbon nitride: rational design and photocatalytic applications for water treatment, *Environ. Sci. Technol.* 50 (2016) 12938–12948.
- [51] L.-L. Feng, Y. Zou, C. Li, S. Gao, L.-J. Zhou, Q. Sun, M. Fan, H. Wang, D. Wang, G.-D. Li, X. Zou, Nanoporous sulfur-doped graphitic carbon nitride microrods: a durable catalyst for visible-light-driven H_2 evolution, *Int. J. Hydrog. Energy* 39 (2014) 15373–15379.
- [52] V.W.-h. Lau, I. Moudrakovski, T. Botari, S. Weinberger, M.B. Mesch, V. Duppel, J. Senker, V. Blum, B.V. Lotsch, Rational design of carbon nitride photocatalysts by identification of cyanamide defects as catalytically relevant sites, *Nat. Commun.* 7 (2016) 12165.
- [53] P. Xia, M. Antonietti, B. Zhu, T. Heil, J. Yu, S. Cao, Designing defective crystalline carbon nitride to enable selective CO_2 photoreduction in the gas phase, *Adv. Funct. Mater.* 29 (2019), 1900093.
- [54] W. Wang, J.C. Yu, D. Xia, P.K. Wong, Y. Li, Graphene and $\text{g-C}_3\text{N}_4$ nanosheets cocrapped elemental α -Sulfur as a novel metal-free heterojunction photocatalyst for bacterial inactivation under visible-light, *Environ. Sci. Technol.* 47 (2013) 8724–8732.
- [55] X. Bai, R. Zong, C. Li, D. Liu, Y. Liu, Y. Zhu, Enhancement of visible photocatalytic activity via $\text{Ag}/\text{C}_3\text{N}_4$ core-shell plasmonic composite, *Appl. Catal. B* 147 (2014) 82–91.
- [56] J. Liu, Y. Liu, N. Liu, Y. Han, X. Zhang, H. Huang, Y. Lifshitz, S.-T. Lee, J. Zhong, Z. Kang, Metal-free efficient photocatalyst for stable visible water splitting via a two-electron pathway, *Science* 347 (2015) 970–974.
- [57] X. Li, S. Wang, H. An, G. Dong, J. Feng, T. Wei, Y. Ren, J. Ma, Enhanced photocatalytic reduction of nitrate enabled by Fe-doped LiNbO_3 materials in water: performance and mechanism, *Appl. Surf. Sci.* 539 (2021), 148257.
- [58] P. Chen, A promising strategy to fabricate the Cu/BiVO_4 photocatalysts and their enhanced visible-light-driven photocatalytic activities, *J. Mater. Sci. Mater. Electron.* 27 (2016) 2394–2403.
- [59] P. Raizada, A. Sudhaik, P. Singh, P. Shandilya, V.K. Gupta, A. Hosseini-Bandegharai, S. Agrawal, Ag_3PO_4 modified phosphorus and sulphur co-doped graphitic carbon nitride as a direct Z-scheme photocatalyst for 2, 4-dimethyl phenol degradation, *J. Photochem. Photobiol. A* 374 (2019) 22–35.
- [60] L. Xu, L. Yang, E.M.J. Johansson, Y. Wang, P. Jin, Photocatalytic activity and mechanism of bisphenol A removal over $\text{TiO}_2-x/\text{rGO}$ nanocomposite driven by visible light, *Chem. Eng. J.* 350 (2018) 1043–1055.
- [61] L. Liu, S.F. Sim, S. Lin, J. Wan, W. Zhang, Q. Li, C. Peng, Integrated structural and chemical analyses for HCl-supported hydrochar and their adsorption mechanisms for aqueous sulfachloropyridazine removal, *J. Hazard. Mater.* 417 (2021), 126009.
- [62] Z. Hou, J. Chu, C. Liu, J. Wang, A. Li, T. Lin, C.P. François-Xavier, High efficient photocatalytic reduction of nitrate to N_2 by Core-shell $\text{Ag}/\text{SiO}_2/\text{eTiO}_2$ with

- synergistic effect of light scattering and surface plasmon resonance, *Chem. Eng. J.* 415 (2021), 128863.
- [63] X. Gu, S. Lu, X. Fu, Z. Qiu, Q. Sui, X. Guo, Carbon dioxide radical anion-based UV/ $S_2O_8^{2-}$ /HCOOH reductive process for carbon tetrachloride degradation in aqueous solution, *Sep. Purif. Technol.* 172 (2017) 211–216.
- [64] P. Chen, L. Blaney, G. Cagnetta, J. Huang, B. Wang, Y. Wang, S. Deng, G. Yu, Degradation of ofloxacin by perylene diimide supramolecular nanofiber sunlight-driven photocatalysis, *Environ. Sci. Technol.* 53 (2019) 1564–1575.
- [65] M. Aono, K. Yoshitake, H. Miyazaki, XPS depth profile study of CZTS thin films prepared by spray pyrolysis, *Phys. Status Solidi C* 10 (2013) 1058–1061.
- [66] Z. Xie, Y. Feng, F. Wang, D. Chen, Q. Zhang, Y. Zeng, W. Lv, G. Liu, Construction of carbon dots modified $MoO_3/g-C_3N_4$ Z-scheme photocatalyst with enhanced visible-light photocatalytic activity for the degradation of tetracycline, *Appl. Catal. B* 229 (2018) 96–104.
- [67] X. She, H. Xu, Y. Xu, J. Yan, J. Xia, L. Xu, Y. Song, Y. Jiang, Q. Zhang, H. Li, Exfoliated graphene-like carbon nitride in organic solvents: enhanced photocatalytic activity and highly selective and sensitive sensor for the detection of trace amounts of Cu^{2+} , *J. Mater. Chem. A* 2 (2014) 2563–2570.
- [68] S. Xiao, D. Zhang, D. Pan, W. Zhu, P. Liu, Y. Cai, G. Li, H. Li, A chloroplast structured photocatalyst enabled by microwave synthesis, *Nat. Commun.* 10 (2019) 1570.